



Improved Quality of Scattering-Coefficient Images via Linear Spatial Deconvolution in Dynamic Diffuse Optical Tomography

H. L. Graber^{1,2}, Y. Xu^{1,2}, Y. Pei², R. L. Barbour^{1,2}

¹Dept. of Pathology / SUNY Downstate Medical Center / 450 Clarkson Ave. Brooklyn, NY 11203; harry.graber@downstate.edu

²NIRx Medical Technologies LLC / 15 Cherry Lane / Glen Head, NY 11545



INTRODUCTION

Diffuse optical tomography (DOT) is a functional imaging modality with great potential utility for studies of human brain function. DOT employs harmless near infrared radiation and yields images of spatially varying tissue absorption and scattering coefficients (μ_a and μ_s), which can be correlated with important physiological parameters. The advantages of DOT include its superior temporal resolution and the greater freedom of movement by the subject that it permits, compared to PET imaging or fMRI. But the image quality that typically is achieved, especially in terms of spatial resolution, is less than desirable. Most previously proposed strategies for improving image quality entail use of computation-intensive algorithms, which minimize the possibility of studying tissue dynamics in a practical time frame.

A sequence of papers from our group has chronicled the development of a computationally efficient strategy for producing DOT images of usefully high quality [1-4]. The key operation is a linear spatial deconvolution; computation of the relevant operator is independent of, and so may precede, collection of experimental data, and the time needed for its application is <1 s. While we have had considerable success with this approach, previous characterizations of it were limited by taking only spatiotemporally varying absorption into account. Here we complement the prior work by examining the ability of the deconvolution strategy to improve the quality of recovered images of the diffusion coefficient D ($\sim 1/\mu_s$).

METHODS

All of the simulations reported here used circular, 4-cm radius, 2D media. The modeled heterogeneities consisted of either one or two circular inclusions wherein D was approximately half that of the background region (i.e., inclusion μ_s is approximately twice that of the background).

Two types of two-inclusion studies were undertaken; in every case the inclusion diameter was fixed at 0.6 cm, with one centered at (x_c, y_c) and the other at $(-x_c, y_c)$. For the first study, y_c was fixed at 0 and x_c was adjusted, in 0.1-cm increments, from a minimum of 0.3 cm (i.e., inclusions have a point of contact) to a maximum of 1.0 cm. For the second, x_c was fixed at 0.5 cm and y_c was adjusted, in 0.2-cm increments, from a minimum of 0.2 cm to a maximum of 3.0 cm. The particular case illustrated in Fig. 1 is $D(x, y)$ for inclusions centered at $(\pm 1, 0)$.

In every simulation, the absorption coefficient was fixed at $\mu_a = 0.06 \text{ cm}^{-1}$ throughout the medium, while the background scattering coefficient was $\mu_s^{\text{bkg}} = 10 \text{ cm}^{-1}$, which, according to the relation $D = 1/[3(\mu_a + \mu_s)]$, correspond to a background diffusion coefficient of $D^{\text{bkg}} = 0.0331 \text{ cm}$. Within the inclusions, the time-averaged scattering coefficients were $\mu_s^{\text{inc}} = 20 \text{ cm}^{-1}$ for all one-inclusion and all noise-free two-inclusion computations, and $\mu_s^{\text{inc}} = 30 \text{ cm}^{-1}$ for the two-inclusion simulations with noise added to the detector data. Dynamic scattering was modeled through the relation $\mu_s^{\text{inc}}(t) = \mu_s^{\text{inc}}[1 + 0.25\sin(2\pi ft)]$, with $f = 0.1 \text{ Hz}$ and $t = 0.5, 1, \dots, 49.5, 50 \text{ s}$. Thus D^{inc} ranges from 0.0139 to 0.0208 cm (0.00924-0.0139 cm for the noise-added two-inclusion case) with a mean value of 0.0170 (0.0113 cm).

All forward-problem and inverse-problem computations were carried out in the manner specified in Ref. 5. Reconstructed images [e.g., Fig. 4(a)-(c), 5(d)-(f)] were post-processed by applying the spatial deconvolution algorithm that was the subject of Refs. 1-4 and Poster 686 T-PM. The key distinction between this report and the previous ones is that here μ_s , rather than μ_a , was modulated in each reference-medium pixel. All modeled $\mu_s(x, y)$ states were converted to the corresponding spatial distributions of D , and the deconvolution operator was generated by comparing the latter to the recovered D images, as explained in Refs. 1-3. To examine the effect of random error on the accuracy of recovered images, computations were conducted three times, with noise-free detector data used in the first instance, and with data to which Gaussian white noise was added in the remainder. The noise levels were 1% and 2%, where the noise level ϵ_k for the k^{th} S-D channel is defined as $\epsilon_k = 100s_k/m_k^{\text{bkg}}$, s_k is the standard deviation of the k^{th} -channel noise distribution, and m_k^{bkg} is the time-averaged noise-free detector reading.

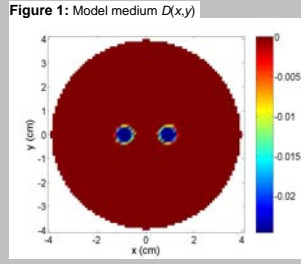


Figure 1: Model medium $D(x, y)$

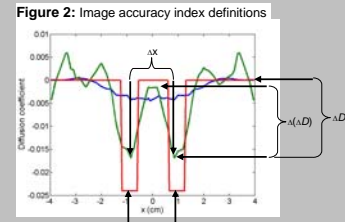


Figure 2: Image accuracy index definitions

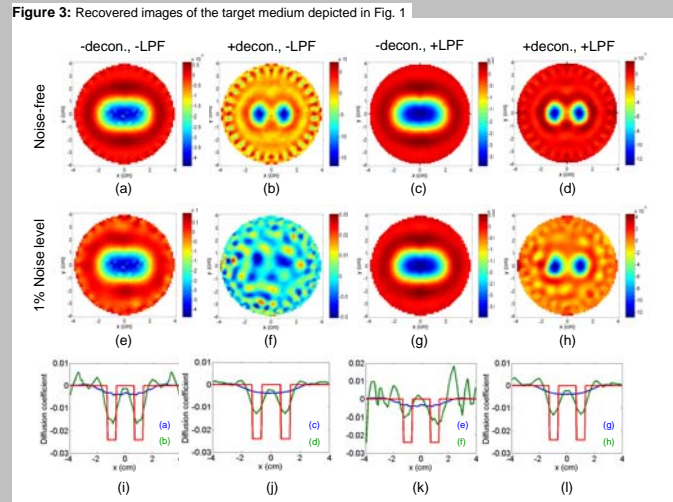


Figure 3: Recovered images of the target medium depicted in Fig. 1

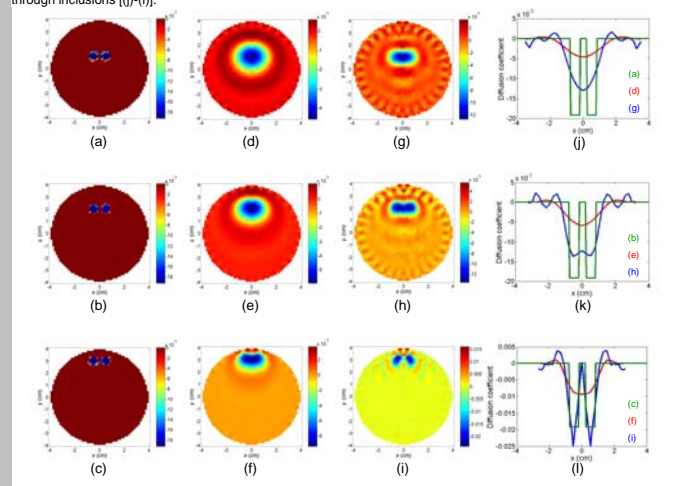


Figure 4: Target media [(a)-(c)], recovered images before [(d)-(f)] and after [(g)-(i)] deconvolution, 1D sections through inclusions [(j)-(l)].

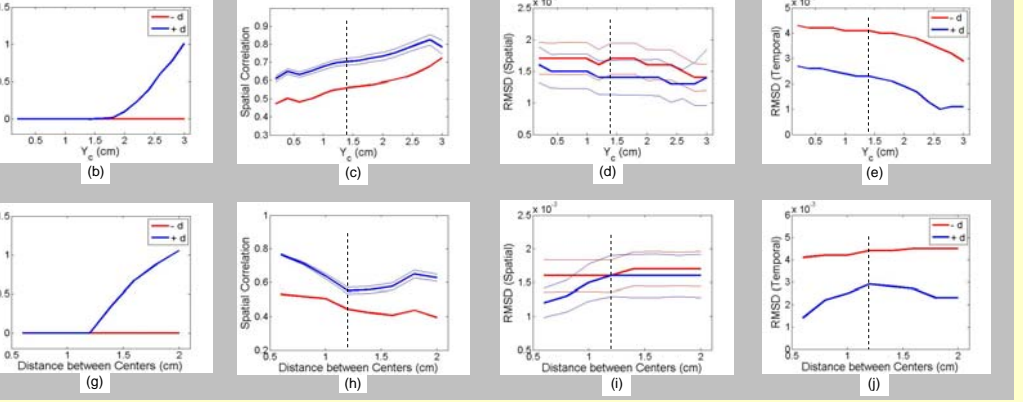


Figure 5: Summary indices of qualitative and quantitative image accuracy

Recovered images were subsequently treated with a noise-suppression scheme consisting of a combination of temporal low-pass filtering (tLPF) and spatial "pillbox" filtering (sLPF) [5]. The spatial and temporal correlation coefficients (SC and TC, respectively), and spatial and temporal root mean squared error (sRMSE and tRMSE, respectively), between target medium and reconstructed images are used here as global indices of spatial and temporal accuracy of recovered images [5]. Several "local" measures of image quality also were computed (see Fig. 5(a)-(d)). The parameters from which the latter were computed are defined in Figure 2.

RESULTS

Representative images and 1D sections for a two-inclusion target medium, time frame and inclusion location $(x_c, y_c) = (\pm 0.9, 0)$, are shown in Figure 3. Qualitatively, the trends and dependencies seen in these results agree with those previously reported for target media containing μ_a perturbations [3]. Most important is that spatial deconvolution yields significantly improved images, in terms of spatial resolving power and quantitative accuracy. Second, deconvolution tends to amplify any background artifacts, whether they originate from systematic factors or from random errors; when the detector data are noisy, the inclusions continue to be recovered with fair accuracy, but the amplitudes of noise artifacts can become comparable to those of the inclusions. Third, by using the tLPF and sLPF in combination [5], the background artifacts are substantially reduced, at the cost of some reduction in quantitative accuracy.

For the Figure 4 results, the center-to-center distance between the inclusions is 1 cm, the detector data are noise-free, and the tLPF and sLPF are not used. The coordinates of the inclusion centers are $(x_c, y_c) = (\pm 0.5, 1)$, $(\pm 0.5, 2)$, or $(\pm 0.5, 3)$. Corresponding 1D sections, along the inclusion bisector, also are shown. Even at their most superficial position, the inclusions are never resolved in the spatially convolved images, while after deconvolution they are partly resolved when $y_c = 2 \text{ cm}$ and fully resolved when $y_c = 3 \text{ cm}$.

Various scalar indices of image accuracy are plotted in Figure 5. Results for the variable- y_c study are in Fig. 5(a)-(e), and those for a complementary variable- x_c (y_c fixed at 0) are in Fig. 5(f)-(j). Neither of the resolving-power indices [Fig. 5(a),(f),(g)] rises above zero for the spatially convolved images. For the deconvolved images, partial resolution is seen when $y_c > 1.4 \text{ cm}$ in Fig. 5(a). The other quantities plotted in Fig. 12 are the SC, sRMSE and tRMSE. The SC is significantly higher, and the tRMSE is substantially lower, after deconvolution than before. Likewise, whenever the sRMSE is different before and after deconvolution, the latter image has the lower value. The vertical dashed lines in Fig. 5 are located at the values of y_c or x_c at which the inclusions begin to be resolved.

CONCLUSIONS

The linear approach to DOT image enhancement described in Refs. 1-4 is as effective at improving the quality of D images as it is for μ_a . The accuracy of the recovered spatial distributions were observed to increase in terms of both resolution and quantitatively. Guided in part by these studies, and those presented in Poster 686 T-PM, we have constructed a series of solid-state dynamic phantom media, the imaging studies so far conducted (manuscript in preparation) indicate that combination of spatial deconvolution and noise suppression operations can produce the same types of image quality improvement when applied to experimental data as they have in simulations.

REFERENCES

- R.L. Barbour, H.L. Graber, Y. Xu, Y. Pei, and R. Aronson, "Strategies for imaging diffusing media," *Transport Theory and Statistical Physics* 33: 361-371 (2004).
- H.L. Graber, Y. Xu, Y. Pei, and R.L. Barbour, "Spatial deconvolution technique to improve the accuracy of reconstructed three-dimensional diffuse optical tomographic images," *Applied Optics* 44: 941-953 (2005).
- Y. Xu, H.L. Graber, Y. Pei, and R.L. Barbour, "Improved accuracy of reconstructed diffuse optical tomographic images by means of spatial deconvolution: two-dimensional quantitative characterization," *Applied Optics* 44: 2115-2139 (2005).
- Y. Xu, Y. Pei, H.L. Graber, and R.L. Barbour, "Image quality improvement via spatial deconvolution in optical tomography: Time-series imaging," *J. Biomedical Optics* 10: 051701 (2005).
- Y. Pei, H.L. Graber, and R.L. Barbour, "Influence of systematic errors in reference states on image quality and on stability of derived information for DC optical imaging," *Applied Optics* 40: 5755-5769 (2001).

This work was supported in part by the National Institutes of Health (NIH) under Grants R41-NS050007 and R41-NS049736, and by the US Army under Grant DAMD17-03-C-0018.